CMS Physics Analysis Summary

Contact: cms-pag-conveners-exotica@cern.ch 2011/07/25

Search for BSM $\mathrm{t\bar{t}}$ Production in the Boosted All-Hadronic Final State

The CMS Collaboration

Abstract

A search is presented for a massive particle or resonance, generically referred to as a Z′, decaying into a $t\bar{t}$ pair. The search focuses on Z′ resonances which are sufficiently heavy to result in energetic top quarks with decay products partially or fully merged into one jet. The analysis relies on new developments in the area of jet substructure and uses those techniques to suppress QCD background. The analysis is performed in proton-proton collisions corresponding to a luminosity of 886 pb^{-1}. Sub-picobarn limits are set on $\sigma_{Z'} \times BR(Z' \to \mathrm{t\bar{t}})$ for Z′ heavier than 1.1 TeV/c^2. A Randall-Sundrum Kaluza-Klein gluon with mass between 1.0 and 1.5 TeV/c^2 is also excluded at 95% C.L.

1 Introduction

A number of scenarios for physics beyond the Standard Model (BSM) feature new gauge interactions with favorable couplings with the third-generation quarks [1–9]. These couplings result in new heavy states, referred to generically as Z', which could appear as resonances in top pair production at the LHC. For example, Ref. [10] shows an example of these heavy states expressed as Kaluza-Klein gluons with concrete predictions of cross sections and branching ratios. Also of note are axigluon models (Refs. [11–15]) that have recently been proposed to solve the discrepancy in the top pair production forward-backward asymmetry from the Tevatron [16–20]. It also has been argued that some axigluon models that can explain the asymmetry have already been excluded by other Standard Model measurements [21], however we are also sensitive to this effect in an independent channel.

Searches for new physics in top pair production have been performed by the Tevatron experiments [22–24]. The Tevatron measurements provide the most stringent lower mass limits for a narrow resonance: indeed, a narrow topcolor leptophobic $\mathrm{t\bar{t}}$ resonance is excluded for masses below about 800 GeV/c^2.

The results presented in this paper are based on approximately 886 pb^{-1} of data collected by the CMS experiment in 2011 at a center-of-mass energy of 7 TeV. The reference model is a Z' with a narrow width (1% of its mass) so the analysis is applicable to any narrow resonance decaying into $\mathrm{t\bar{t}}$ [25]. The analysis sets model-independent limits on the production cross section for such particles as a function of the resonance mass $m_{Z'}$.

This study focuses on $Z' \to \mathrm{t\bar{t}}$ in the all-hadronic channel, taking advantage of its large branching ratio (46%), and in particular in resonances that are heavier than about 1 TeV/c^2, as this region has not been explored by the Tevatron experiments. In addition, due to a large QCD background, an all-hadronic search is not very sensitive at lower Z' masses. Finally, our approach relies on specific techniques in jet reconstruction which can powerfully suppress the QCD, but only in the kinematic region where the top quarks are sufficiently energetic.

This analysis exploits the highly-boosted nature of the top quarks from the high-mass resonances, namely the fact that the top quark decay products often fall inside a single jet. If the boost is not too large, the decay products are distinguishable in this jet (in particular, the W boson decay products), and this information can be used to reduce the large generic QCD dijet production. These decay products within the jet are referred to as "subjets".

A *top tagging algorithm* [26, 27] is used to identify merged top jets by analyzing their substructure. This is accomplished by examining the clustering sequence of the jets, and the application of specialized selection criteria. The behavior of jets from heavy particles such as top quarks is different from generic QCD jets. For instance, QCD jets tend to have very few subjets within them, whereas the jets that originate from hadronic top decays have three or four subjets. Furthermore, the kinematics of these subjets is different. While the subjets of generic QCD jets tend to be close together and one often dominates the jet energy (due to gluon emission in the final state), the top quark decay products share the jet energy more equally and emerge at wider angles.

The masses involved in the process (the top mass and the W mass) also give strong handles for such discrimination. The mass of a typical QCD jet exhibits a falling spectrum after a quick initial rise (Ref. [28]), whereas the mass of a fully merged jet from a top quark is very close to the top mass (170-175 GeV/c^2). It is often possible to identify two of the subjets within the top jet as coming from the decay of the W. Similarly to the mass of the entire jet, for generic QCD jets the mass of this W candidate has a falling spectrum in the region of interest, whereas the

W decay products from the sequential top decay are very close to the W mass.

For situations where the decay products of the top quark are not contained entirely in one jet, we have also developed a technique to discriminate against QCD backgrounds using similar techniques as described for the fully-merged case. However, for this purpose we deploy a tool that is able to handle more general topologies than the "top jet tagger" targeted specifically at the hadronic top decays.

The *jet pruning algorithm*, presented in Ref. [29, 30], can be used to identify substructure from general topologies. While this tool has been shown to be slightly less performant on fully boosted top jets than the targeted top jet tagger, it is of more general utility for arbitrary topologies. Ref. [31] has detailed algorithmic comparisons of the taggers for fully boosted top systems, and for instance, for the same efficiency to identify true top quarks, the probability to misidentify a generic QCD jet with the jet pruning algorithm is larger by 20-30% than the targeted top jet tagger.

On the other hand, the targeted top tagging tool is not applicable to moderately boosted top quark systems where not all of the decay products are merged, and as such, we have made use of the jet pruning tool to develop an algorithm that identifies boosted hadronically-decaying W-bosons into one jet (referred to as a W jet). In this case, we make use of the fact that the decay products from generic QCD jets are radiated fairly asymmetrically, whereas the decay products from the W are more symmetric because they arise from a two-body decay of W boson. We then construct top quark candidates by combining this W jet with another jet that is close to it, and form a full top quark candidate.

2 Analysis Strategy

The events of interest are classified into three categories depending on the boost of the top quark and the impact of that boost on the merging of its decay products. This analysis is based on dividing the event into hemispheres, so that each hemisphere encompasses the final decay products from each top. This way the $\mathrm{t\bar{t}}$ pair is fully reconstructed. In all of the regions of interest, it is assumed that the $\mathrm{t\bar{t}}$ system has sufficient energy to boost the decay products of each top into a single hemisphere, namely that $E_{\mathrm{t}} > 2 \times m_{\mathrm{t}}$. Because of this, the total energy of the event must be $E_{\mathrm{t\bar{t}}} > 4 \times m_{\mathrm{t}}$; as a consequence, this analysis is very inefficient at energies below ~ 750 GeV/c^2, and for this reason we do not evaluate upper limits below 1 TeV/c^2.

Depending on the amount of merging of top decay products, two hemisphere types are considered in this analysis:

1. High boost, where all three jets in one hemisphere are merged into a single "hard" jet. The mass of this hard jet, often denoted "top jet" throughout this note, is usually similar to the mass of the top quark, and will have three or more subjets. We denote this topology a "Type 1" hemisphere (which refers to the number of total jets, in this case one).

2. Moderate boost, where all of top quark's decay products lie in a hemisphere, but only two out of three jets are merged. Very often the jets that merge are the daughters of the W, which also form a "hard" jet, but this time with a mass similar to that of the W. This "W jet" usually has only two subjets. In this case, the top quark candidate is reconstructed by adding a neighboring jet from the same hemisphere which is expected to be from the b-quark. (If a tighter selection is needed, this jet is also required to be b-tagged.) This is referred to as a "Type 2" hemisphere because there are two jets in it.

For the purposes of this analysis, a hemisphere is defined by the leading jet's transverse momentum vector. Jets that fall within $\Delta\phi < \pi/2$ of this jet are considered within the leading hemisphere, and jets that fall outside $\Delta\phi >= \pi/2$ are considered within the subleading hemisphere.

The $Z' \to t\bar{t}$ search is performed in two "channels":

- The "type 1+1" channel is a dijet event (one jet in each hemisphere), in which each jet is a "type 1" hemisphere passing the top tagging selection.
- The "type 1+2" channel is a trijet event (one jet in one hemisphere, and two jets in the other). In this case, we identify the "type 1" hemisphere as the hemisphere containing the leading jet with $p_T > 350$ GeV/c. The Type 1 hemisphere contains a fully merged top candidate, denoted the "Type 1 Top Candidate". The remaining jets are assigned to two hemispheres based on their azimuthal angle relative to the "Type 1 Top Candidate". If the relative azimuthal angle of a jet is more than $\frac{\pi}{2}$, it is included in the "Type 2 hemisphere." The Type 2 hemisphere has a W jet candidate (the leading jet in the "Type 2 Hemisphere") and an additional nearby jet, which is the b jet candidate. The combination of the W and b jet candidates is denoted as the "Type 2 Top Candidate".

Since the experimental signature of this analysis is high p_T jets, the main backgrounds to this analysis are:

- QCD multijet production, and
- Continuum SM $t\bar{t}$ production.

At the Z' resonance masses considered in this analysis, the SM $t\bar{t}$ component is significantly smaller than the QCD contribution. The irreducible SM $t\bar{t}$ background is estimated from Monte Carlo simulation (and includes systematic errors related to Monte Carlo modeling). Since the QCD background dominates, both "1+1" and "1+2" channels use data-driven techniques to estimate it.

After comparing the data against the combined background prediction, we extract the limit on the production cross-section of Z' as a function of its mass.

3 CMS Detector

The CMS detector [32] is a general-purpose device, however it has many features particularly suited for reconstruction of energetic jets, in particular the finely segmented electromagnetic and hadronic calorimeters and the charged particle tracking. The charged particles are reconstructed by the inner tracker, immersed in a 3.8 T axial magnetic field; the inner tracker consists of three layers and two endcap disks of pixel sensors, and ten barrel layers and twelve endcap disks of silicon strips. This arrangement results in a full azimuthal coverage within $|\eta| < 2.5$, where η is the pseudorapidity and is defined as $\eta = -\ln\tan(\theta/2)$. The CMS uses a polar coordinate system, with the z axis coinciding with the axis of symmetry of the CMS detector, and oriented in the counterclockwise proton direction; here θ is the polar angle defined with respect to the positive z axis. The pseudorapidity is an approximation for the full rapidity y, and the approximation is exact for massless particles. Since many of the particles we use are not massless, we use the full rapidity y which is defined as

$$y = \frac{1}{2}\frac{E + p_z/c}{E - p_z/c}. \quad (1)$$

A lead-tungstate crystal electromagnetic calorimeter (ECAL) and a brass-scintillator hadronic calorimeter (HCAL) surround the tracking volume and allow photon, electron and jet reconstruction up to $|\eta| = 3$. The ECAL and HCAL cells are grouped into towers projecting radially outward from the interaction region. In the central region ($|\eta| < 1.74$) the towers have dimensions $\Delta\eta = \Delta\phi = 0.087$; however, at higher η, the $\Delta\eta$ and $\Delta\phi$ widths increase. ECAL and HCAL cell energies above the noise suppression thresholds are combined within each tower to define the calorimeter tower energy, and the towers are further combined into clusters, which are then identified as jets. For an improved jet reconstruction, the tracking and calorimeter information is combined in an algorithm called particle-flow [33], which is described below.

4 Data Sample and Event Selection

4.1 Simulated and Collision Data Samples

The data sample was collected in 2011 at $\sqrt{s} = 7$ TeV and corresponds to an integrated luminosity of 886 pb^{-1}. We use events triggered by a single hadronic calorimeter jet. As the instantaneous luminosity increased with time, two different thresholds were used in different time periods. Initially, at least one calorimeter jet with $p_{\mathrm{T}} > 240$ GeV/c. For most of the data taking, the threshold was raised to 300 GeV/c. Offline, we require that one jet satisfies $p_{\mathrm{T}} > 350$ GeV/c. The efficiency of these triggers after applying a loose preselection is over 95% for invariant masses above 1.5 TeV/c^2. However, there is still a small effect from the trigger turn-on for invariant masses below 1.5 TeV/c^2. We account for it in the simulation and have cross-checked with a data-driven technique to ensure that the Monte-Carlo-derived efficiency is correct.

To simulate the SM background processes, the MadEvent/MadGraph [34] and PYTHIA6 [35] event generators are used. Top pair production is described with the use of MadGraph, and includes spin correlations in the top decays. Higher order gluon and quark production is described via matrix elements (ME) with up to three extra jets beyond the top quark pair system. The chosen threshold for the parton-shower to matrix-element matching is 30 GeV.

MadGraph was also used to produce the model of a generic high mass resonance decaying to top pairs. In particular, a model with a Z′ that has the same fermion couplings as the SM Z, and masses between 1 and 3 TeV/c^2 was implemented. Note that in the generation of the Z′ model, its decay is forced into a pair of top quarks. The width of the resonance was set to 1% of $m_{Z'}$, to make it smaller than the expected experimental resolution.

The events were fully simulated and reconstructed via the CMS simulation and reconstruction software.

4.2 Jet Reconstruction and Event Preselection

Event data are reconstructed using the particle-flow reconstruction algorithm [33], which attempts to reconstruct all stable particles in an event by combining information from all subdetectors. The algorithm categorizes all particles into five types: muons, electrons, photons, charged and neutral hadrons. The resulting particle flow candidates are passed to each jet clustering algorithm to create "particle flow jets".

The particle flow candidates are clustered using the Cambridge-Aachen (CA) jet clustering algorithm [36, 37], as implemented in FastJet version 2.4.2 [38, 39].

Charged hadrons identified as pileup are removed from the inputs to the jet clustering algorithms. The charged hadrons are classified as belonging to a pileup vertex when they are used

to reconstruct a vertex that is not the highest p_T primary vertex. Furthermore, charged leptons with an isolation of 15% (muons) or 20% (electrons) of the lepton transverse momentum are also removed, where the isolation is defined as the fraction of energy from charged particles, neutral particles, and photons (counted separately).

After these subtractions, only the neutral component of pileup remains; it is removed by applying a residual area-based correction as described in Ref. [40, 41]. The mean p_T per unit area is computed with the k_T algorithm with the "active area" method, with a distance parameter of 0.6, and the jet energy is corrected by the amount of pileup expected in the jet area. The "active area" method adds a large number of infinitely soft "ghost" particles to the clustering sequence to examine which jet they are clustered into, and the area is computed by the set of points for each jet. η-dependent jet corrections are also necessary, due to the different responses in the endcap and barrel calorimeters. The amount of energy expected from underlying event is added back into the jet. The pileup-subtracted jet four momenta are finally corrected for nonlinearities in η and p_T with simulated data, with a residual η-dependent correction added to correct for the difference in simulated and true responses [42]. Constituents of the jet (i.e. subjets) are not corrected, and algorithmic procedures are done on uncorrected jet energies.

The corrections for the CA $R = 0.8$ jets are derived from studies using the anti-k_T $R = 0.5$ jet algorithm. Simulation studies confirm that they work well for the jet momenta considered here. A further description of additional jet energy corrections due to using jet substructure techniques is described below.

The following preselection is applied. The events must have a good primary vertex as computed by a deterministic annealing filter (DAF). Furthermore, beam backgrounds are removed by requiring that events with at least 10 tracks have at least 25% of the tracks satisfying high purity tracking requirements. The "type 1 + 1" events are required to have at least two jets reconstructed with the top tagging algorithm with $p_T > 350\,\text{GeV}/c$, $|y| < 2.5$, with jet identification selection applied. The "type 1 + 2" events are required to have at least three jets. The leading jet is constructed with the top tagging algorithm and must have $p_T > 350\,\text{GeV}/c$. The second jet is constructed with the jet pruning algorithm and must have $p_T > 200\,\text{GeV}/c$. The third jet is also constructed with the jet pruning algorithm and must have $p_T > 30\,\text{GeV}/c$. All jets must satisfy a $|y| < 2.5$ requirement, and pass the same jet identification selection as the "type 1 + 1" case.

4.3 The Top Tagging and W Tagging Algorithms

The products of hadronic decays of top quarks or W bosons can fall within a single jet if these particles are boosted relative to their mass. The top and W tagging algorithms are developed to identify these boosted top and W jets [43].

Figure 1 (taken from Ref. [43]) shows the efficiency of the top tagging and W tagging algorithms. For instance, with the top tagging algorithm, a top tagging efficiency of over 40% for jets with $p_T > 600$ GeV/c is obtained (where p_T is the momentum of the jet transverse to the beam axis). In this paper, it will be shown that we reject about 95% of light jets (for $p_T \sim 600$ GeV/c).

4.3.1 Top tagging algorithm

In the top tagging algorithm, Cambridge-Aachen $R = 0.8$ jets are used as inputs (where $R = \sqrt{\Delta\eta^2 + \Delta\phi^2}$), as described in Section 4.2. The input CA jets are hereby referred to as the "hard jets." The algorithm has two steps: the primary decomposition, in which the algorithm attempts to split the hard jet into two subjets, and the secondary decomposition, in which

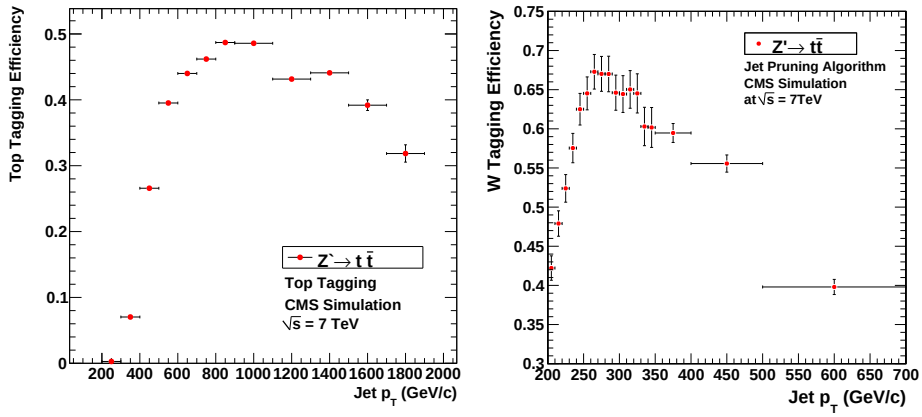

Figure 1: Expected efficiency of the top (left) and W (right) tagging algorithms as derived from Ref. [27].

the algorithm attempts to split the subjets found by the primary decomposition. In the process, soft and wide-angle particles (relative to the parent in the clustering) are ignored. At least three subjets are required. The following variables, defined for each jet passing the algorithm, are used to tag top jets:

- **Jet Mass** m_{jet} - The mass of the four-vector sum of the constituents of the hard jet.
- **Number of Subjets** N_{subjets} - The number of subjets found by the algorithm.
- **Minimum Pairwise Mass** m_{min} - The three highest p_{T} subjets are taken pairwise, and each pair's invariant mass is calculated via $m_{ij} = \sqrt{(E_i + E_j)^2 - (\vec{p}_i + \vec{p}_j)^2}$. m_{min} is the mass of the pair with the lowest invariant mass ($m_{\text{min}} = \min[m_{12}, m_{13}, m_{23}]$). This variable is not defined for jets with less than three subjets.

Jets that have mass close to the top mass, at least three subjets, and minimum pairwise mass close to the W mass are tagged as top jets. Specifically:

$$140 < m_{\text{jet}} < 250\,\text{GeV}/c^2 \tag{2}$$
$$N_{\text{subjets}} \geq 3 \tag{3}$$
$$m_{\text{min}} > 50\,\text{GeV}/c^2 \tag{4}$$

4.3.2 W tagging algorithm

The jet pruning algorithm also uses the Cambridge-Aachen $R = 0.8$ jets as inputs, described in Section 4.2. In contrast to the top tagging algorithm, the jet pruning algorithm reclusters the jet starting from the constituents, but again removes soft and wide-angle clusters. The same parameters are chosen for the jet pruning algorithm as in the original theoretical papers [29, 30]. The following selection is also applied, which exploits the variables used in Ref. [44]:

- **Number of Subjets** N_{subjets} - Require two subjets in the pruning algorithm.
- **Pruned Jet Mass** m_{jet} - Require the total pruned jet mass to satisfy $60\,\text{GeV}/c^2 < m_{\text{jet}} < 100\,\text{GeV}/c^2$.
- **Mass Drop** - The subjet mass is used to sort the two subjets. By looking at the last clustering iteration of the pruned jet, the *mass drop* of the hardest subjet (hereby referred to as 1), and is required to satisfy $\frac{m_1}{m_{\text{jet}}} = \mu < 0.4$. The mass drop requirement

ensures that the mass of the jet is roughly evenly spread between two or more subjets.

These criteria are designed to select W candidates in which the daughter subjets are similar in energy and mass.

5 Algorithmic Characterization

In order to use the substructure tools that we have presented in the previous section, it is necessary to measure several supporting numbers. The first is the subjet energy scale. The second is the selection efficiency of the substructure tools in the data (compared to the Monte Carlo). The third is the rate at which generic QCD jets fake the selection (the "mistag rate").

5.1 Subjet energy scale

It is conceivable that the subjet energy scale is different from the energy scale of the total jet, and that the simulation we are using is not capturing this effect. In order to estimate this, we have investigated the effects of substructure in a lepton-plus-jets $t\bar{t}$ sample which has a boosted W jet, with a luminosity of 490 pb^{-1} (this is different from the full analysis because the later part of the data has a more complicated trigger schema that impacts the analysis). We compare the peak of the W mass distribution to the true value of the W mass before and after the ordinary jet energy corrections and apply a residual correction to account for the differences.

These semileptonic events are then separated into two hemispheres to take advantage of the boosted nature of the final state. A very strong jet p_T cut will ensure that this happens. Each hemisphere will roughly contain the decay products from one top quark. The advantage of doing this is that there is less ambiguity in the decay products of each top quark.

The hemispheres are defined by the lepton. We define the "semileptonic hemisphere" as the hemisphere containing the lepton, and the "hadronic hemisphere" as the opposite one.

The events are selected with one isolated muon consistent with originating from the collision primary vertex and with $p_T > 45\,\text{GeV}/c$ and $|\eta| < 2.1$; no other isolated electrons or muons with $p_T > 45$ GeV and $|\eta| < 2.1$ are allowed.

The event selection is then required to have ≥ 2 jets with $p_T > 30\,\text{GeV}/c$, ≥ 1 jet with $p_T > 200\,\text{GeV}/c$, ≥ 1 jet tagged with a secondary vertex b tagging algorithm, and ≥ 1 jet in the hadronic hemisphere passing the mass drop cut $\mu < 0.25$.

We then plot the highest mass in the hadronic hemisphere in Figure 2. The data are shown in points, the $t\bar{t}$ Monte Carlo is in red, the W+jets Monte Carlo is in green, and a QCD multijet background is shown in yellow (the latter is determined by fits to the transverse mass distribution). Figure 3 shows a plot of the mass of the "type 2" top candidate, formed by adding the closest jet to the "type 2" W candidate. Only events in a W mass window of 60-100 GeV/c^2 are considered.

A fit to a combined Gaussian plus exponential for the data is shown as a solid line, and a fit to a combined Gaussian plus exponential for the Monte Carlo is shown as a dashed line.

The results are:

$$m_W^{\text{DATA}} = 82.8 \pm 2.4\ \text{GeV}/c^2 \quad (5)$$

$$m_W^{\text{MC}} = 82.0 \pm 2.2\ \text{GeV}/c^2 \quad (6)$$

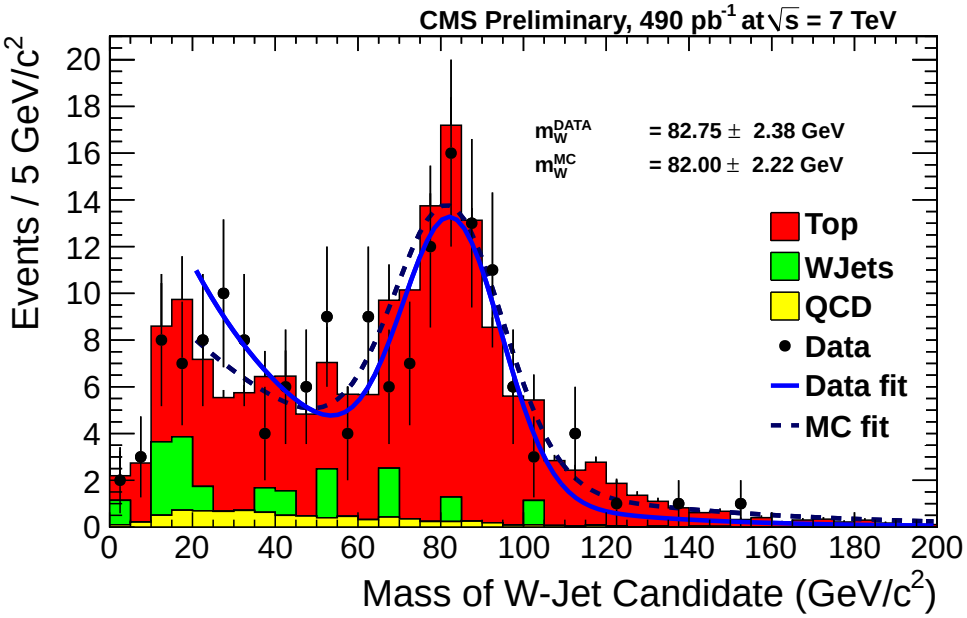

Figure 2: Mass of the highest mass jet in a semileptonic top sample.

Thus, the subjet energy scale scale factor for W jets is determined to be 1.01 ± 0.04. The top mass is measured to be

$$m_t^{\mathrm{DATA}} = 176 \pm 6 \text{ GeV}/c^2 \quad (7)$$

$$m_t^{\mathrm{MC}} = 171 \pm 5 \text{ GeV}/c^2 \quad (8)$$

Only the statistical uncertaintis are quoted for these measurements.

Because the kinematic threshold for top jets to fully merge is rather high, there are very little data left after the strong p_T cuts, and too little data are left to isolate a fully-merged ("type 1") top jet sample.

In order to proceed, we make a simplifying assumption that the ratio between the jet energy scale in data and the jet energy scale in Monte Carlo is the same between the W tagger and the top tagger. Our previous studies of QCD jets [43] suggest that this is a reasonable assumption within the large uncertainties quoted already.

Conservatively, we thus apply an additional uncorrelated 5% uncertainty in addition to the uncertainties of the standard jet correction uncertainties (described in Section 4.2). This is applied for both the top tagging and jet pruning algorithms.

5.2 Substructure Selection Efficiency

The selection efficiency of the substructure algorithms (top tagging and W tagging) can in principle be different between data and simulation. In order to estimate the size of this effect, we again examine the semileptonic sample described in the previous section, and look at the sequential selection of the jet pruning algorithm in data and simulation in order to estimate the difference in efficiency for the W tagging algorithm. There are no statistics available for the top tagging in the semileptonic sample, and so we make the assumption that the "ratio of efficiencies" between data and Monte Carlo (i.e. the data-to-Monte-Carlo *scale factor*) is the same for the W and top tagging algorithms.

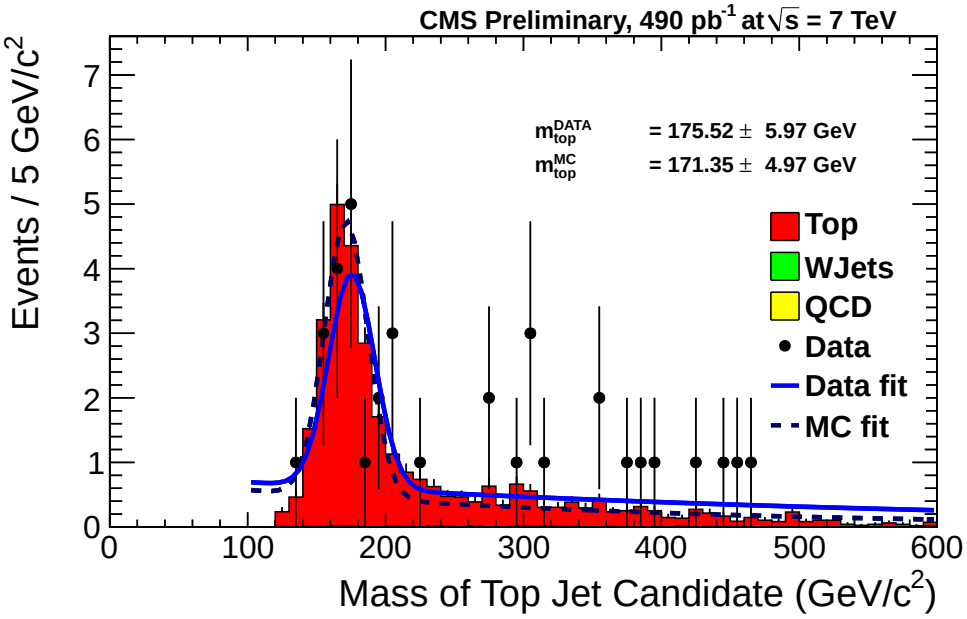

Figure 3: Mass of the hadronic top candidate in a semileptonic top sample.

Figure 4 shows the mass drop (μ) variable immediately before the W mass selection. The selection efficiencies for the data and Monte Carlo are

$$\epsilon_{\mu}^{\mathrm{DATA}} = 0.56 \pm 0.03 \quad (9)$$

$$\epsilon_{\mu}^{\mathrm{MC}} = 0.61 \pm 0.03 \quad (10)$$

Using Figure 2 to investigate the data and Monte Carlo efficiencies of the W mass-window cut, we obtain

$$\epsilon_{m_{\mathrm{W}}}^{\mathrm{DATA}} = 0.50 \pm 0.04 \quad (11)$$

$$\epsilon_{m_{\mathrm{W}}}^{\mathrm{MC}} = 0.50 \pm 0.04 \quad (12)$$

Combining the efficiencies of the μ and mass cuts, the subjet energy scale scale factor is determined to be 0.93 ± 0.13. This is applied as an additional systematic uncertainty on the selection efficiency.

5.3 Mistagging Rate

The mistagging rate is derived from data. However, *a priori*, the rates may depend on the sample composition of the two different analyses considered (1+1 and 1+2). Thus, we derive the mistag rate in both samples independently, and apply the rates to the appropriate analysis (1+1 rate to 1+1 analysis, and likewise for 1+2).

We estimate the mistag rate (P_{m}) which is the probability that a QCD jet will be mistaken for a top jet candidate by the top tagging algorithm. Highly energetic QCD jets have a larger probability to radiate, and as the jet mass increases, they are more likely to have top-like substructure

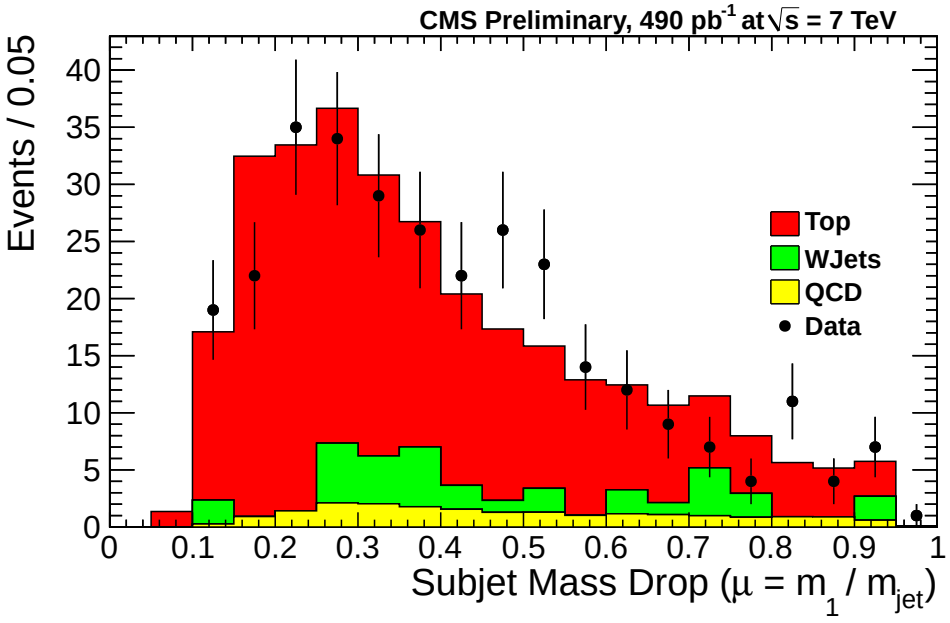

Figure 4: Mass drop of the highest mass jet in a semileptonic top sample. The luminosity is 490 pb^{-1}.

(and thus 'fake' a top tag). Ref. [28] has a phenomenological explanation for this effect using NLO predictions of jet masses, for instance. For this reason the mistag rate is a function of the jet p_{T} , $P_{\text{m}}(p_{\text{T}})$.

The mistag rate for the "1+1" analysis is determined from data by the following procedure:

1. We take a dijet event with both jets above the threshold.
2. We randomly pick one jet.
3. We require that the jet satisfy the jet mass criterion of the top tag, but explicitly fails the substructure cuts. That is, we require
   - $140 < m_{jet} < 250\,\text{GeV}/c^2$ AND
   - ($N_{subjets} < 3$ OR $m_{min} < 50\,\text{GeV}/c^2$).

   A majority of the events in which the jet fails one of these two criteria are QCD; we call it an 'anti-tag'. The opposite-side jet is thus likely to be a QCD jet with the kinematics similar to the signal sample, hence the ensemble of these jets is an excellent control region. We call these opposite side jets "probe jets".
4. We then ask whether the probe jet is tagged. The fraction of probe jets which are tagged (in a given p_{T} range) defines the mistag rate.
5. The small ($< 10\%$) contribution from continuum $\text{t}\bar{\text{t}}$ is removed based on the Monte Carlo expectation.

The mistag rate as a function of jet p_{T} is shown in the red circles in Fig. 5.

The mistag rate for the "1+2" analysis is determined from a procedure analogous to the "type 1 + 1" case. The same mistag parameterization technique is used, using the "type 1" hemisphere.

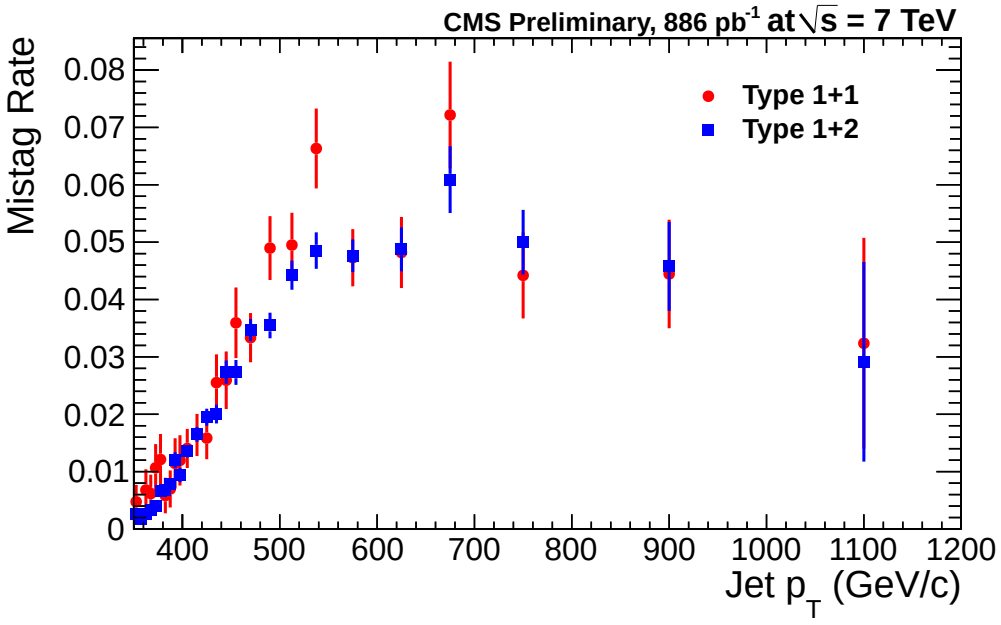

Figure 5: Top tagging mistag rate derived from dijet data (red circles) versus trijet data (blue squares), following the 'anti-tag and probe' procedure, as explained in the text. The rate derived from dijet data is applied to the "Type 1 + 1" analysis, whereas the rate derived from trijet data is applied to the "Type 1 + 2" analysis. There is a small ($< 5\%$) contribution from continuum $t\bar{t}$ production that is removed, using the expectation from Monte Carlo.

However, because the quark/gluon fractions can be different (*a priori*) for dijet events (as in the "1+1" analysis) and trijet events (as in the "1+2" analysis), the mistag rate must be separately derived for the "1+2" analysis.

The mistag rate for trijet events is determined from data by the following procedure:

1. We select trijet events with the leading three jets passing the thresholds 350, 200, and 30 GeV/c respectively. No requirements are made on the jet masses for the "Type 1 Top Candidate" nor the W candidate, and no requirements are made on the invariant mass of the "Type 2 Top Candidate".

2. The "Type 1" top candidate is then used as a "probe jet".

3. As in the "1+1" case, the top tagging rate of the probe jet is taken as the mistag rate for the algorithm. Because no selection criteria are made on the masses of the "Type 2 Top Candidate", nor the "W candidate", this is still dominated by QCD in the right kinematic regime, and is therefore an appropriate control region from which to derive the mistag rate.

4. The small contribution from continuum $t\bar{t}$ is removed based on the Monte Carlo expectation.

The mistag rate as a function of jet p_{T} for trijet events is shown in the blue squares in Fig. 5.

6 High Mass Search

The search for a 'high-mass' Z' boson decaying into $t\bar{t}$ is performed using the "Type 1+1" topology, assuming both top quarks decay hadronically and their decay products merge into a single jet. Therefore, the search is performed in dijets which are near or above the top jet merging threshold.

The signal consists of events where both energetic jets are also top tags. Figure 6 shows the expectation from Monte Carlo of the reconstructed $t\bar{t}$ invariant mass distribution for various prototypical Z' signals with masses from 1 to 3 TeV/c^2. We search for a Z' peak on top of a falling background, which is a mixture of QCD and Standard Model $t\bar{t}$.

The signal efficiency is estimated from the Monte Carlo, with several scale factors applied. The first weighting procedure is to account for the trigger inefficiency. As described in Section 4, we account for the trigger turnon with a weighting procedure derived from the Monte Carlo. The second is a scale factor accounting for the difference between the observed efficiencies of the substructure selection in data and Monte Carlo, derived below in Section 5.2. The value is 0.86 ± 0.24 (this number is equal to the single tag scale factor squared, since we are taking two tags in each event).

Sample	p_T >350 GeV/c	$\|\eta\| < 2.4$	$\Delta\phi > 2.1$	$140 < m_{\text{jet}} < 250$ GeV/c^2	$N_{\text{subjets}} > 2$	$m_{\text{min}} > 50$ GeV/c^2
Z' (1 TeV/c^2)	17%	17%	17%	3%	2%	2%
Z' (1.5 TeV/c^2)	46%	46%	46%	16%	10%	8%
Z' (2 TeV/c^2)	61%	61%	61%	24%	14%	11%
Z' (3 TeV/c^2)	59%	59%	58%	22%	12%	8%

Table 1: Summary of cumulative 1 + 1 signal selection efficiencies for major selection criteria of various Z' masses.

The continuum $t\bar{t}$ contribution is small and is estimated from the Monte Carlo simulation. The same scale factor of 0.86 ± 0.26 is applied to the $t\bar{t}$ Monte Carlo, similarly to the Z' signal.

The QCD background is estimated from data using the mistag rate derived in Section 5.3. Dijet events are used to estimate and model the QCD background in the invariant mass distribution of the two top candidates. First, one of the jets is randomly selected and required to be top tagged. This subsample of events with a single tag is still completely dominated by QCD jets. A "probe jet" is defined as the other jet in the event (in the hemisphere opposite to the tagged jet).

The single tag sample is dominated by QCD events in which probe jets originate from light quarks or gluons and typically have a low jet mass. However, the events in the signal region are required to have jet masses consistent with top quark mass, in a window between 140 and 250 GeV/c^2. As $m_{t\bar{t}}$ computed from two jets depends on their masses, if one were to use the original low mass of the probe jet in the background estimate, the shape of the estimated $m_{t\bar{t}}$ distribution would not be correct.

In order to mimic the event kinematics of the signal region, the jet mass of the probe jet is ignored, and instead the jet mass is set to a random number drawn from a flat probability distribution function (chosen for simplicity) of jet masses from 140 to 250 GeV/c^2. This new "mass-modified-mistag" is used in the construction of the invariant mass distribution of the candidate $t\bar{t}$ pair. This ensures that the mass of the probe jet is at least roughly similar to the mass of the equivalent jet from the signal region.

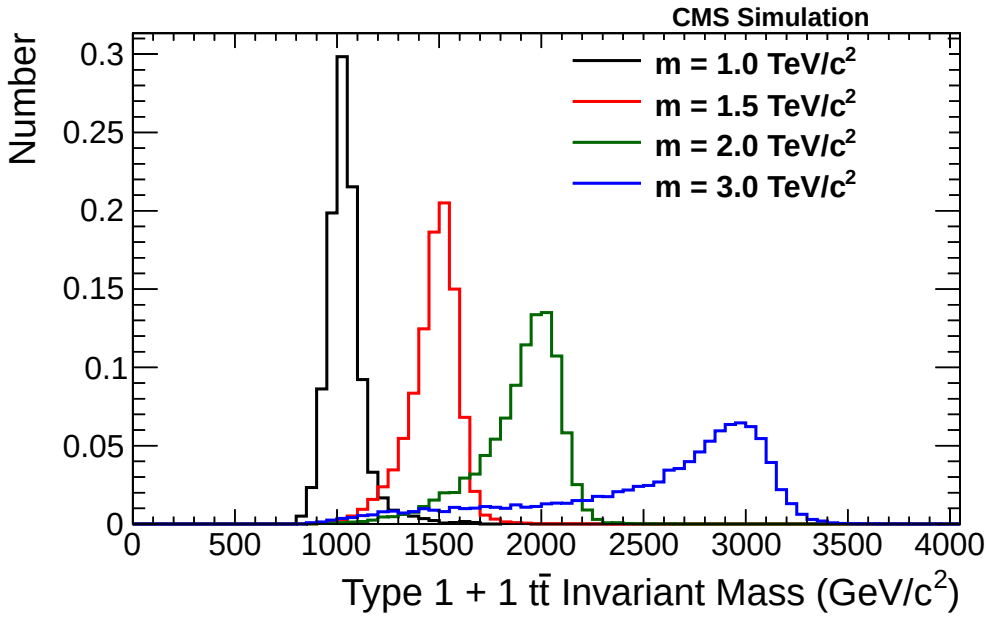

Figure 6: The shapes of four Z′ signals (for four different masses) for the "Type 1 + 1" analysis obtained from the Monte Carlo simulation.

As a closure test of this procedure, it is performed on a QCD MC sample. Figure 7 shows the observed and predicted distributions. The mistag rate is derived from even events in MC, and applied to the odd events in the same MC sample using the "mass-modified-mistag" procedure. The agreement in QCD MC is good, within the statistical uncertainty.

Given the p_{T} of the probe jet, we obtain the mistag rate from the parameterized function described in Section 5.3. The mistag rate is then used as the weight for the event when filling the "1 + 1" candidate invariant mass distribution (using the "mass-modified" probe jet mass). The resulting QCD distribution is shown as the yellow filled histogram in Fig. 8. The Standard Model $\mathrm{t\bar{t}}$ estimate is shown as a red filled histogram, and the data are shown as solid black points. The hatched gray boxes indicate the total uncertainty on the backgrounds.

The uncertainty on this procedure is taken as half the difference between the "mass-modified-mistag" jet mass, and the true jet mass in the parameterization. Since the fully selected events have a mass requirement on the jets, the true mass of the jets in the parameterization will necessarily be a strict underestimate of the background process in the signal region, and hence the "mass-modified" probe jet mass gives a better estimate. However, this estimates the size of the uncertainty we expect by using a separate probability distribution function for the jet mass of the probe jets.

7 Intermediate Mass Search

The intermediate mass search looks for events with a boosted top jet in one hemisphere, and a boosted W jet plus an additional jet in the other hemisphere, as described in Section 2. Events failing the selections of the high-mass analysis are used in this analysis. This search is sensitive at the lower end of the invariant mass spectrum, however at the higher end of the spectrum the selection efficiency is very low due to jets merging into the "type 1 + 1" case. For this reason, only Z′ masses from 1-2 TeV/c^2 are considered.

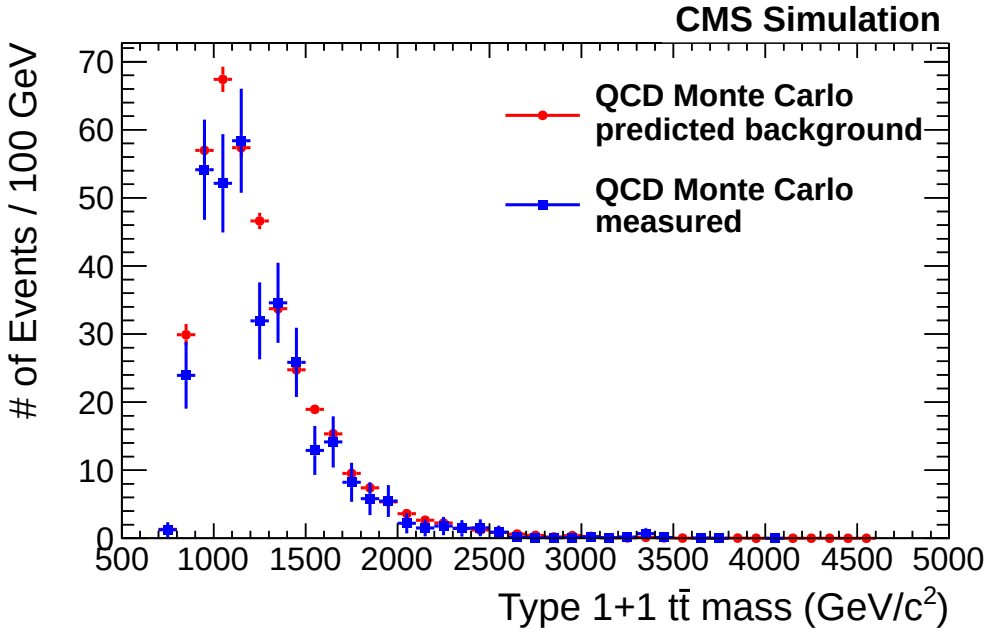

Figure 7: Closure test of the "mass-modified-mistag" prediction. Here, the mistag rate is derived from even events in MC, and applied to the odd events in the same MC sample using the "mass-modified-mistag" procedure.

The "Type 1 Top Candidate" is required to satisfy the top tagging requirements outlined in Section 4.3.1.

The "type 2" hemisphere is required to have the "W candidate" satisfy the "W-jet" tagging criteria described in Section 4.3.2. Furthermore, the nearest jet to the W candidate is combined with the W candidate, and the mass of that "Type 2 Top Candidate" (see Section 2 for the definition) is required to fall within a top mass window. No b tagging requirement is applied on the additional jet to enhance the signal reconstruction efficiency.

On top of the kinematic selection, signal events are selected by requiring that the "Type 1 Top Candidate" pass the top tagging requirements, and that the W candidate pass the W tagging requirements. Furthermore, the invariant mass of the "Type 2 Top Candidate" has to be consistent with the top mass, $140\,\mathrm{GeV}/c^2 < m(\mathrm{jet2},\mathrm{jet3}) < 250\,\mathrm{GeV}/c^2$. The Z′ mass is reconstructed by taking the invariant mass of the "Type 1" and "Type 2" top candidates. Figure 9 shows the reconstruction of Z′ mass with various Z′ mass hypotheses from simulated data.

The signal efficiency is estimated from the Monte Carlo, with several scale factors applied. The first weighting procedure is to account for the trigger inefficiency. As described in Section 4, we account for the trigger turnon with a weighting procedure derived from the Monte Carlo. The second is a scale factor accounting for the difference between the observed efficiencies of the substructure selection in data and Monte Carlo, derived above in Section 5.2. The value is 0.86 ± 0.24.

The Standard Model $\mathrm{t\bar{t}}$ background is also estimated from Monte Carlo simulation, scaled to the theoretical cross section. The same scaling factors as in the Z′ samples (trigger inefficiency and substructure selection) are also applied to the $\mathrm{t\bar{t}}$ Monte Carlo.

Table 2 shows the cumulative selection efficiencies for the Z′ signal with various mass hypotheses. For the very high mass regime, the "1+2" topology loses efficiency which is gained by the

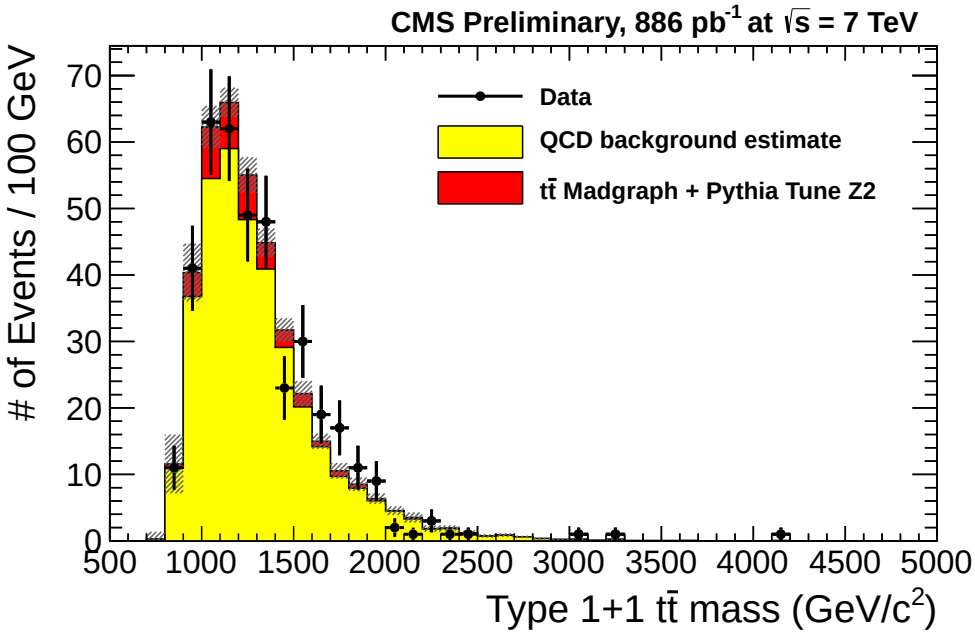

Figure 8: Results of "type 1 + 1" high mass event selection and background estimates. The yellow histogram is the QCD estimate from the data-driven technique described in the text, and the red histogram is the estimate from $t\bar{t}$ continuum production. A data-to-Monte-Carlo scale factor of 0.86 ± 0.24 is also applied to the $t\bar{t}$ Monte Carlo to account for differences in the jet substructure algorithms in a semileptonic $t\bar{t}$ control sample. The black points are the data. The shaded gray boxes indicate the statistical and systematic uncertainty on the total background estimate. The errors shown are not an accurate representation of the background uncertainty in the counting experiment, as they do not take into account events moving in and out of the signal window.

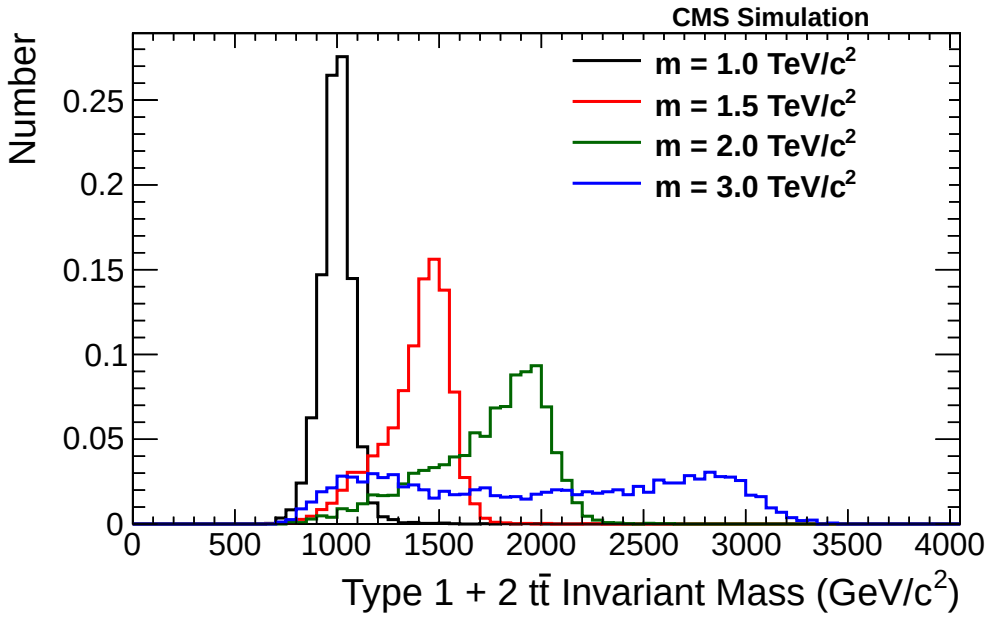

Figure 9: The shapes of four Z′ signals (for four different masses) for the "Type 1 + 2" analysis obtained from the Monte Carlo simulation.

"1+1" topology due to jet merging.

Z′ Sample Mass (GeV/c²)	$p_T^1 > 350$ GeV/c	≥ 2 jets in Type 2 hemis.	"Type 1" extra jets veto	$p_T^W > 200$ GeV/c	$p_T^b > 30$ GeV/c	$\mu < 0.4$	Top Tag	Type 2 Top	Veto Type 1+1
1000	44%	32%	32%	25%	20%	14%	4%	3%	3%
1500	74%	48%	47%	40%	31%	19%	9%	3%	3%
2000	83%	53%	53%	47%	37%	21%	10%	3%	2%

Table 2: Summary of cumulative 1 + 2 signal selection efficiencies for major selection criteria of various Z′ masses.

QCD multijet events are the dominant background of this analysis. The mistag rate for "1 + 2" events is estimated as described in Section 5.3. This is then applied to a QCD control sample, weighting the events to get an estimate of the QCD background in the signal region.

The control region for the QCD background is constructed as follows. The full "Type 2" selection described above is required (with the mass requirements on the W jet, and the "Type 2 Top Candidate") but no requirements are made on the "Type1" hemisphere. The ensemble of "Type 1" candidates in this selection also exhibits the incorrect jet mass compared to the "true" background in the kinematic region of interest (with the jet mass between $140 < m_{\text{jet}} < 250$ GeV/c²). Thus, the same "mass-modified-mistag" procedure is followed as in the "Type 1 + 1" case, and we draw a random mass from a flat probability distribution function between 140 and 250 GeV/c².

The uncertainty on this procedure is taken (as in the "Type 1 + 1" case) as half the difference between the "mass-modified" and true $t\bar{t}$ invariant mass distributions. For the same reasons as in the "Type 1 + 1" case, this is a good estimate of the systematic uncertainty of this procedure.

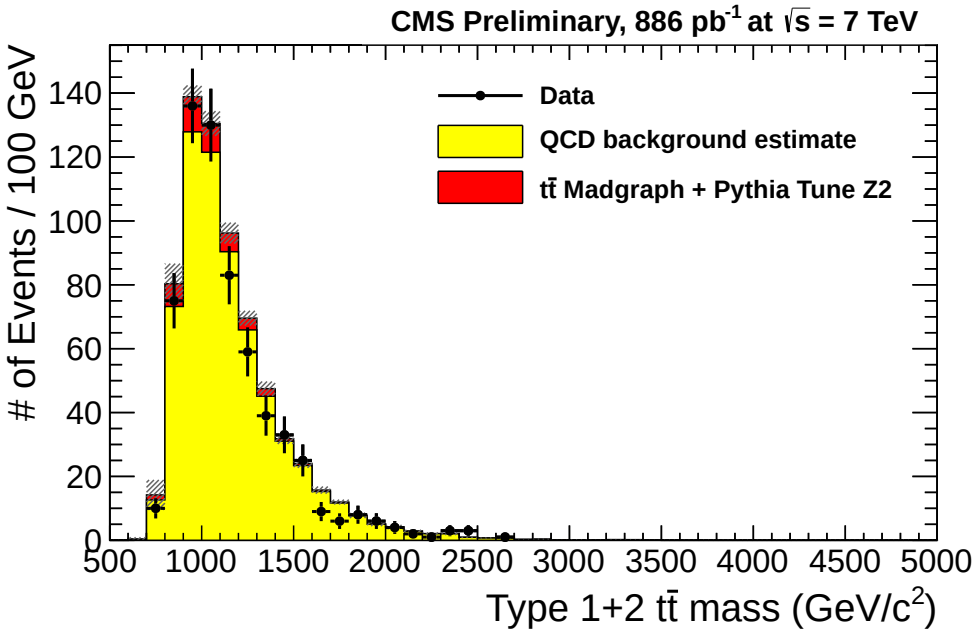

Figure 10: Results of "type 1 + 2" medium mass event selection and background estimates. The yellow histogram is the QCD estimate from the data-driven technique described in the text, and the red histogram is the estimate from $t\bar{t}$ continuum production. A data-to-Monte-Carlo scale factor of 0.86 ± 0.24 is also applied to the $t\bar{t}$ Monte Carlo to account for differences in the jet substructure algorithms in a semileptonic $t\bar{t}$ control sample. The black points are the data. The shaded gray boxes indicate the statistical and systematic uncertainty on the total background estimate. The errors shown are not an accurate representation of the background uncertainty in the counting experiment, as they do not take into account events moving in and out of the signal window.

The results of the event selection are shown in Figure 10. The data-driven QCD background estimate outlined above is in yellow. The $t\bar{t}$ contribution (described above) is in red. The hatched gray boxes indicate the total uncertainty on the backgrounds.

8 Systematic Uncertainties

The sources of systematic uncertainties on the invariant mass spectrum are discussed in this section. They fall into three categories: uncertainties on the efficiency determination; uncertainties on the fake rate determination; uncertainties on the invariant mass distribution. Several sources of systematic uncertainties affect more than one of these three categories and so in those cases the variations are done in a correlated way. The uncertainties on the efficiency determination include uncertainties in overall hard jet energy scale and resolution, subjet energy scale, energy resolution, and angular resolution. There may be additional systematic effects in the subjet quantities that are not present in the hard jet. These systematic effects are investigated below and summarized in Table 3. In order to estimate the uncertainty due to hard jet and subjet energy scales, the energy is increased and decreased, and the effect is checked in the Monte Carlo. This effect is also propagated to the full invariant mass spectrum in a correlated way. The largest systematic uncertainty on the signal acceptance is the subjet energy scale uncertainty.

Resonance Mass Mass Window		M=1.0 0.9-1.1	M=1.5 1.2-1.6	M=2.0 1.3-2.4	M=3.0 2.0-3.3
Source	Variation	Effect (All values in percent)			
Type 1 + 1					
Statistical		2.0	0.9	0.7	0.05
Trigger		13	0.7	0.2	0.1
Subjet selection "scale factor"	93 ± 13	28	28	28	28
Jet energy scale	$\approx \pm 6$	19	6	2	7
Jet energy resolution	10 ± 10	< 1	< 1	< 1	< 1
Jet angular resolution	10 ± 10	< 1	< 1	< 1	< 1
Luminosity	± 6	6	6	6	6
Type 1 + 2					
Statistical		1.6	1.5	1.6	2.5
Trigger		19.5	4.8	3.0	1.9
Subjet selection "scale factor"	93 ± 13	28	28	28	28
Jet energy scale	$\approx \pm 6$	19	6	2	7
Jet energy resolution	10 ± 10	< 1	< 1	< 1	< 1
Jet angular resolution	10 ± 10	< 1	< 1	< 1	< 1
Luminosity	± 6	6	6	6	6

Table 3: Summary of relative systematic uncertainties for the signal efficiency in a mass window. All values are in percent.

Table 4 summarizes the relative systematic uncertainties on the background estimation N_B.

8.1 Jet energy scale

The subjet energy scale is derived for the jet pruning algorithm in Section 5.1. An additional 5% uncertainty is measured for the subjet energy scale, which is added in quadrature to the uncertainties of the overall jet energy corrections described in Section 4.2. We thus vary the four momenta of the jets and subjets up and down by this quadrature-summed amount and investigate the effect on the final result. Since we are performing a counting experiment, the relevant effect is the change in the expected number of events in the signal window. The relative change in event yields is then taken as a systematic uncertainty. The jet energy scale uncertainties in Tables 3 and 4 show a nontrivial dependence on the invariant mass of the postulated resonance because of these effects. For the first mass point (1 TeV/c^2), the signal window is rather small, and hence the effect of changing the jet energy scale is large. As the mass is increased this effect lessens. However, at the very last mass point (3 TeV/c^2), the uncertainty rises again, this time due to the radiative tail of the distribution seen in Figure 6. Changes in the jet energy scale impact the tail of the distribution differently than the core, and hence the effect is magnified.

Resonance Mass		M=1	M=1.5	M=2.0	M=3.0
Mass Window		0.9-1.1	1.2-1.6	1.3-2.4	2.0-3.3
Source	Variation	Relative Effect (All values in percent)			
Type 1 + 1					
$t\bar{t}$ Monte Carlo					
Monte Carlo Statistics	N/A	5	5	5	24
JEC	$\approx \pm 6$	3	28	40	53
Trigger	See text	13	2	1	<1
Substructure tagging scale factor	93 ± 13	28	28	28	28
Luminosity	$\pm$ 6	6	6	6	6
$t\bar{t}$ cross section	$\pm$ 12	12	12	12	12
Total		33	42	51	66
QCD					
QCD prediction statistical	N/A	2	2	2	5
Mistag kinematics	See text	25	5	3	1
Total		25	5	4	5
Total					
$t\bar{t}$ weight		11	10	8	3
QCD weight		89	90	92	97
Total background		22	7	5	6
Type 1 + 2					
$t\bar{t}$ Monte Carlo					
Monto Carlo Statistics	N/A	4	6	8	71
JEC	$\approx \pm 6$	3	28	40	53
Trigger	See text	24	7	7	<1
Substructure tagging scale factor	93 ± 13	28	28	28	28
Luminosity	$\pm$ 6	6	6	6	6
$t\bar{t}$ cross section	$\pm$ 12	12	12	12	12
Total		39	42	51	93
QCD					
QCD prediction statistical	N/A	1	2	2	5
Mistag kinematics	See text	1	5	3	2
Total QCD prediction		2	5	4	5
Total					
$t\bar{t}$ weight		7	4	3	< 1
QCD weight		93	96	97	100
Total background		3	5	4	5

Table 4: Summary of statistical and systematic relative uncertainties for the background estimation in a mass window. The uncertainty for the mistag kinematics is taken as half the difference between the procedure when the "mass-modified-mistag" rate is used, and if the observed jet mass is used. The uncertainty for the trigger selection is taken as half the difference between a Monte-Carlo-derived trigger efficiency weighting scheme, and the raw Monte Carlo efficiency. This is also cross-checked in the data, and the uncertainties assigned cover the differences observed. All values are in percent.

8.2 Jet energy resolution

The jet energy in the simulation is slightly too optimistic, at around the 10±10% level. Thus, we smear the jet energies in the simulation by a factor of 10% for the central value, and use 0% and 20% as uncertainties. At the present time, the subjet angular resolution is taken to be the same as the hard jet and are varied with that assumption. There is no significant effect.

8.3 Jet angular resolution

Similar to the jet energy resolution, the jet angular resolution is also investigated. The variation of the subjet angular resolution is taken to be a variation of 0%, 10%, and 20%. At the present time, the subjet angular resolution is taken to be the same as the hard jet and are varied with that assumption. There is no significant effect.

8.4 Substructure Selection Efficiency

The efficiency of the substructure selections is outlined above, in Section 5.2. Since we are using two substructure tags in both the "1+1" and "1+2" analyses, the uncertainty on the signal efficiency (and the $t\bar{t}$ background Monte Carlo estimate) is twice the efficiency derived in Section 5.2. Thus, the scale factor due to substructure selection efficiency for the analysis is 0.86 ± 0.24.

8.5 Trigger Efficiency

The trigger efficiency impacts the $t\bar{t}$ continuum background, as well as the Z' signal samples. The trigger efficiency is determined from Monte Carlo, and cross-checked using a data-driven technique. The difference between MC and data is approximately a half of the trigger inefficiency estimated in MC. Half of the trigger inefficiency is taken as an estimate of the systematic uncertainty.

9 Statistics

We derive the 95% C.L. upper limit on the product of production cross-section of $Z' \to t\bar{t}$ and its branching fraction to $t\bar{t}$ final state, for both 1+1 and 1+2 channel individually, and for their combination.

In a counting experiment, the number of observed events, N_{obs}, is compared against the expectation based on the production cross section, $\sigma_{Z'}$, its branching ratio, $BF(Z' \to t\bar{t})$, its efficiency $\tilde{\epsilon}$, integrated luminosity, $\tilde{L} = \int \mathcal{L} dt$, and the predicted number of background events, $\tilde{B}$:

$$N_{exp} = \sigma_{Z'} \times BF(Z' \to t\bar{t}) \times \tilde{\epsilon} \times \tilde{L} - \tilde{B}$$

and the likelihood is computed using the Poisson probability to observe N_{obs} given a mean of N_{exp}, with nuisance parameters $\tilde{L}$, $\tilde{\epsilon}$ and $\tilde{B}$.

For each of the signal peaks shown in Figure 9, and for each channel, we

- Define the signal region in $m_{t\bar{t}}$ space. The signal regions are defined in Table 5.
- Integrate the background estimate from Figs. 8 and 10, including its error, and obtain $B \pm \sigma_B$
- Obtain the overall signal efficiency (including acceptance) ϵ and its overall uncertainty σ_ϵ
- Count the observed number of events in this region, N_{obs}.

Z' mass	Lower bound	Upper bound
750	600	1100
1000	900	1100
1250	1000	1400
1500	1200	1600
2000	1300	2400
3000	2000	3300

Table 5: Signal windows for each resonance mass

The total integrated luminosity, common for all signal masses and channels, is $L = 886 \pm 53$ pb^{-1}.

For each Z' mass and each channel, we compute the 95% Bayesian credible interval for $\sigma_{Z'} \times BF(Z' \to t\bar{t})$ in a counting experiment. We assume a flat prior for $\sigma_{Z'} \times BF(Z' \to t\bar{t})$, and log-normal priors for the nuisance parameters $\tilde{B}$, $\tilde{\epsilon}$, and $\tilde{L}$, with respective log-normal means and sigmas of $B \pm \sigma_B$, $\epsilon \pm \sigma_\epsilon$, and $L \pm 0.06 \times L$.

For each value of Z' mass, we also report a combination of the two counting experiments from "1+2" and "1+1" channels. This is performed by forming a joint likelihood, where only $\sigma_{Z'} \times BF(Z' \to t\bar{t})$ and the integrated luminosity (with 6% relative error) are considered common to both channels. Since the amount of Standard Model $t\bar{t}$ is small, we neglect its correlation between the channels and add it to the uncorrelated QCD background estimate. We also neglect the correlation in the signal efficiency (*e.g.*, from the substructure scale factor, trigger efficiency, etc.) for simplicity

10 Results

Following the Bayesian technique described in Sec. 9, the limit from the joint likelihood of two counting experiments is shown in Fig. 11, which is our main result. Also shown in blue is the prediction of a topcolor Z' model from Ref. [25] for widths of 1.2% and 3%, and the expectation from a Kaluza-Klein gluon from Ref. [10], updated to 7 TeV via private communication with the authors. The detailed inputs for the limits are shown in Table 6.

11 Cross Checks

In the semileptonic sample used to compute the subjet jet energy scale and the substructure data-to-MC efficiency scale factor, many boosted W jets are observed. However, no fully merged top jets are observed (i.e., no "type 1" hemispheres) due to small statistics. As a check of observations of the "type 1" hemispheres, an additional b tag is required on the b jet candidate in the "1 + 2" analysis. While the efficiency and background estimates for this procedure have not been adequately determined at the present time, from MC estimates a "true $t\bar{t}$ " purity of more than 60% is expected. In this sample, 40 events are observed, of which a high fraction are predicted to be boosted continuum $t\bar{t}$. These events are tagged by three separate algorithms: the top tagging algorithm, the W tagging algorithm, and the b tagging algorithm.

One of these "golden" events is selected for graphical display. Figure 12 shows a fully annotated $\rho - \phi$ view. Figure 13 shows the same event with the particle flow candidates fully drawn, in the $\rho - \phi$ view, and Figure 14 shows the particle flow candidates in the lego view.

Z' mass	Signal window	ϵ_{MC}	ϵ_{trig}	ϵ_{total}	$\sigma_{\epsilon_{total}}$	B	σ_B	N_{obs}
Type 1 + 1								
1000	900-1100	1.2%	79.2%	0.8%	0.3%	102.6	22.9	104
1100	900-1200	2.9%	83.1%	2.1%	0.7%	168.6	23.7	166
1200	900-1300	4.2%	86.9%	3.1%	1.0%	223.6	23.3	215
1300	1000-1400	5.2%	90.8%	4.1%	1.3%	228.1	11.0	222
1400	1100-1500	6.3%	94.7%	5.2%	1.6%	197.6	10.6	182
1500	1200-1600	7.1%	98.6%	6.1%	1.7%	153.7	9.7	150
1600	1200-1700	7.9%	98.8%	6.7%	1.9%	168.8	10.8	169
1800	1200-2000	10.0%	99.2%	8.5%	2.4%	194.2	11.6	206
1900	1200-2200	10.5%	99.4%	9.0%	2.6%	202.2	11.7	209
2000	1300-2400	10.8%	99.6%	9.3%	2.6%	151.0	8.1	164
2100	1300-2400	10.6%	99.6%	9.1%	2.6%	151.0	9.1	164
2200	1400-2500	10.1%	99.6%	8.7%	2.5%	107.3	5.8	117
2300	1500-2600	9.6%	99.6%	8.3%	2.3%	76.3	3.8	94
2400	1700-2700	8.9%	99.7%	7.6%	2.1%	40.1	2.0	45
2500	1700-2800	8.5%	99.7%	7.4%	2.1%	40.7	2.0	45
2600	1700-2900	8.4%	99.7%	7.2%	2.0%	41.0	2.0	45
3000	2000-3300	6.9%	99.8%	5.9%	1.7%	16.4	0.9	10
Type 1 + 2								
1000	900-1100	2.1%	71.9%	1.3%	0.5%	269.4	8.7	266
1100	900-1200	3.2%	75.8%	2.1%	0.7%	365.6	15.6	349
1200	900-1300	3.2%	79.7%	2.2%	0.8%	435.2	19.5	408
1300	1000-1400	3.1%	83.5%	2.3%	0.8%	343.7	21.4	311
1400	1100-1500	3.0%	87.4%	2.3%	0.8%	245.0	15.4	214
1500	1200-1600	2.6%	91.3%	2.1%	0.6%	172.9	9.2	156
1600	1200-1700	2.8%	91.9%	2.2%	0.6%	188.6	9.6	165
1700	1200-1900	2.8%	92.5%	2.3%	0.7%	208.4	10.5	179
1800	1200-2000	2.7%	93.1%	2.2%	0.6%	213.5	10.4	185
1900	1200-2200	2.6%	93.8%	2.1%	0.6%	220.5	10.8	191
2000	1300-2400	2.2%	94.4%	1.8%	0.5%	155.1	6.2	136

Table 6: Signal efficiency, expected background event counts, and number of observed events in the signal window for each Z' mass point. The signal efficiency is broken up into the Monte Carlo efficiency ϵ_{MC}, the trigger efficiency ϵ_{trig}, and the total signal efficiency $\epsilon_{total} = C_{tag}^2 \epsilon_{MC} \epsilon_{trig}$, where C_{tag} is the scale factor described in section 8. The signal efficiency uncertainty $\sigma_{\epsilon_{total}}$ is described in Table 3. The number of expected background events B and its uncertainty σ_B are described in Table 4. N_{obs} is the number of events observed in data.

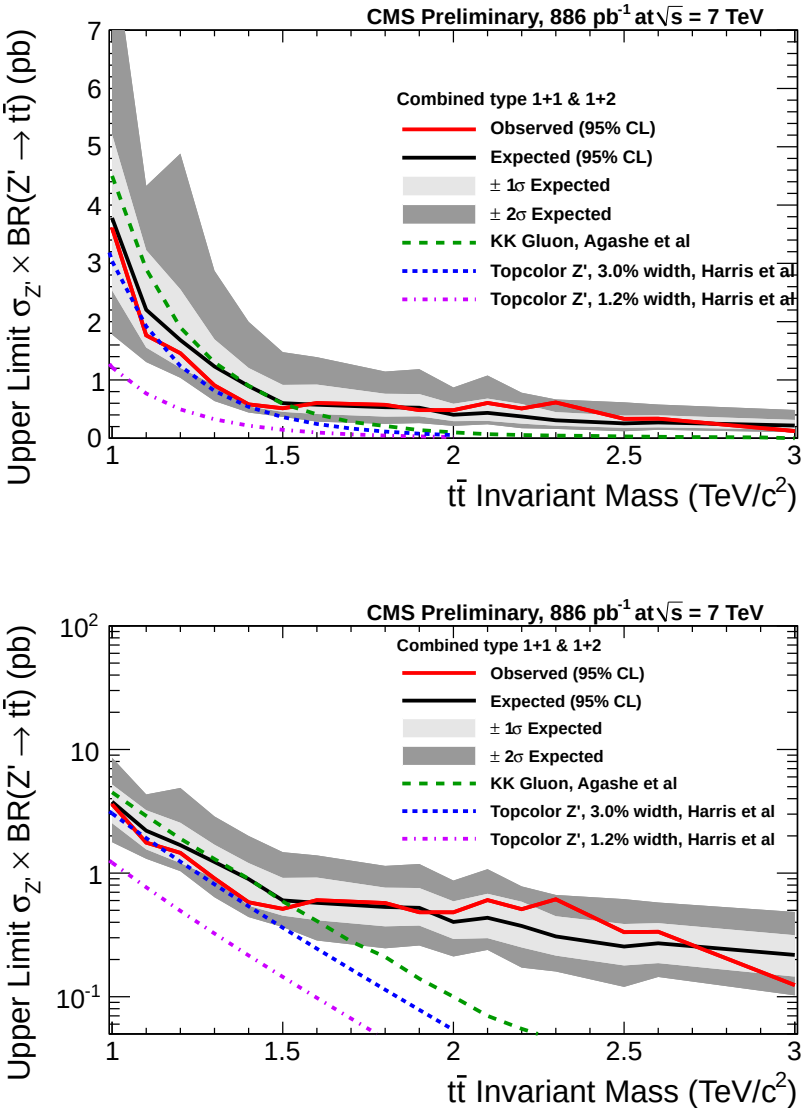

Figure 11: The 95% C.L. upper limit on a product of the production cross section of Z' and a branching fraction for its decay into $t\bar{t}$ pair, as a function of assumed Z' mass, for a combination of "1+2" and "1+1" channels. The limits are evaluated using a Bayesian procedure, integrated with Markov Chain MC. Three theoretical models are examined in shades of purple. From top to bottom: a Kaluza-Klein gluon from Ref. [10], updated to 7 TeV via private communication with the authors (Note: the KK gluon model has a width larger than that of the signal Monte Carlo); a topcolor Z' model from Ref. [25] with width 3%; and a topcolor Z' model from Ref. [25] with width 1.2%. (a) linear scale (b) log scale.

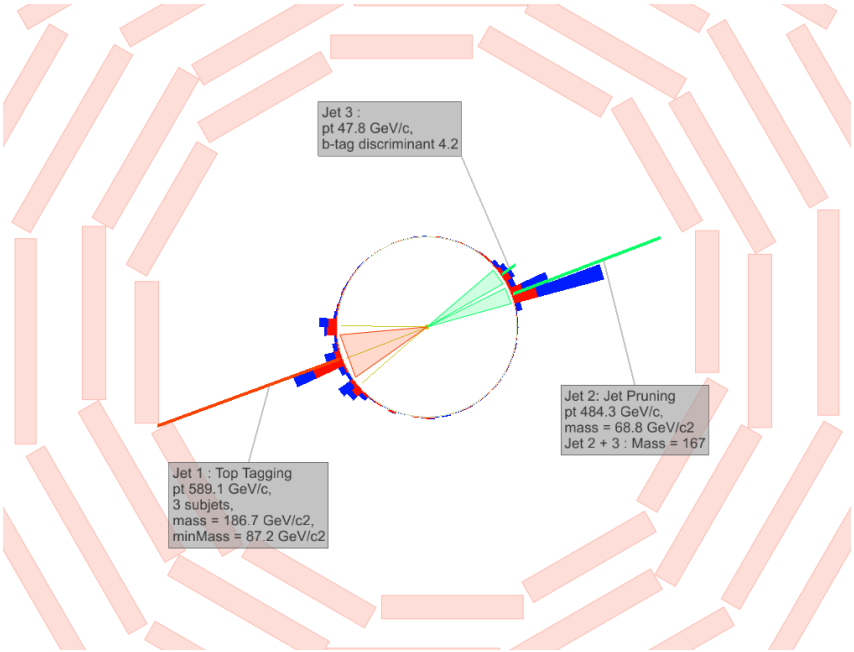

Figure 12: Event display of a "golden" triply-tagged "1 + 2" candidate. The invariant mass of the $t\bar{t}$ candidate is 1352.5 GeV/c^2. In addition to the analysis selection, an additional b tagging requirement is made on the candidate b jet in the "type 2" hemisphere. The "type 1" top jet is shown in orange, with yellow denoting the three subjets. The "type 2" hemisphere jets are shown in green. Jet 2 is tagged with the W tagging algorithm, and Jet 3 is tagged with a secondary vertex tag. The electromagnetic calorimeter information is shown in red, and the hadronic calorimieter information is shown in blue.

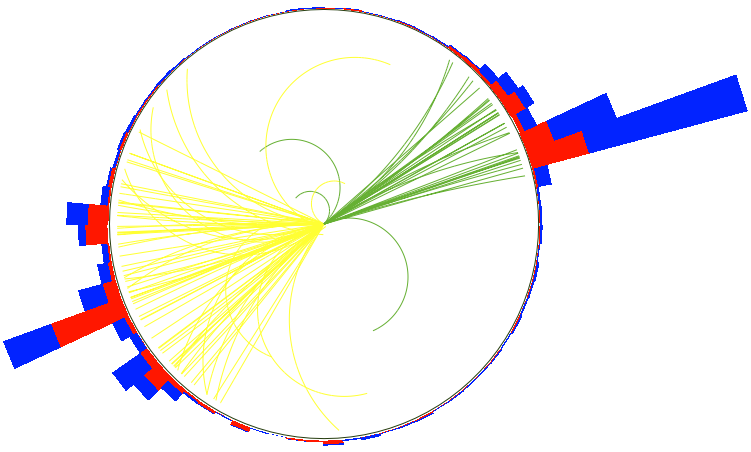

Figure 13: Event display of a "golden" triply-tagged "1 + 2" candidate. In addition to the analysis selection, an additional b tagging requirement is made on the candidate b jet in the "type 2" hemisphere. Here, the yellow corresponds to the particle flow candidates of the "type 1" hemisphere jets, and the green corresponds to the particle flow candidates of the "type 2" hemisphere jets. The lines are charged and neutral particles. The electromagnetic calorimeter information is shown in red, and the hadronic calorimieter information is shown in blue.

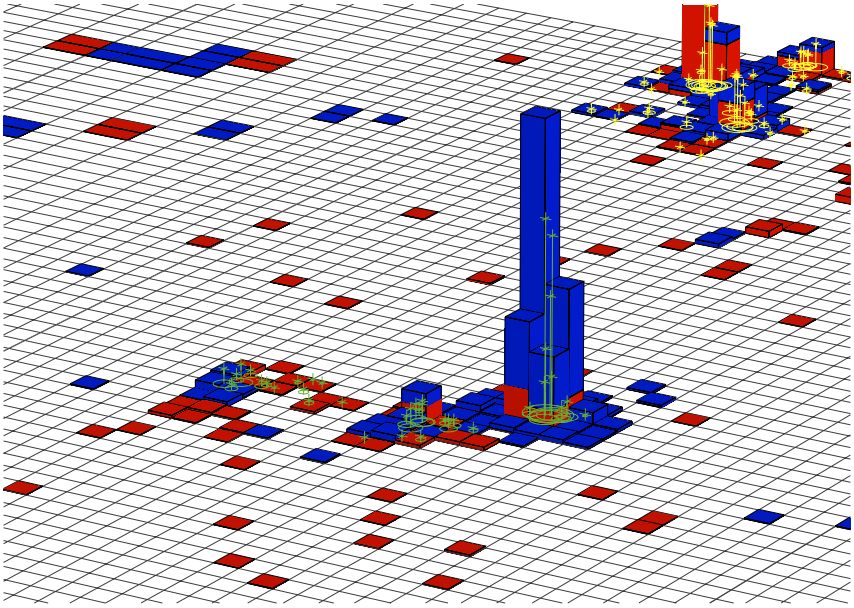

Figure 14: Event display of a "golden" triply-tagged "1 + 2" candidate. In addition to the analysis selection, an additional b tagging requirement is made on the candidate b jet in the "type 2" hemisphere. Here, the yellow corresponds to the particle flow candidates of the "type 1" hemisphere jets, and the green corresponds to the particle flow candidates of the "type 2" hemisphere jets. The height of the line is the energy measured by the particle flow algorithm for the various particles. The lines are charged and neutral particles. The electromagnetic calorimeter information is shown in red, and the hadronic calorimieter information is shown in blue.

12 Conclusions

In conclusion, we have searched for a heavy resonance decaying into a $t\bar{t}$ pair. As a straw-man model of such a resonance, we consider a narrow Z'. Our search focused on Z' masses which are sufficiently large to result in top quarks which are very energetic and thus whose decay products invariably partially or fully merge into one jet. We thus rely on new developments in the area of jet substructure and use it to suppress QCD backgrounds. After analyzing 886 pb^{-1} of CMS data from 2011, we set sub-picobarn limits on $\sigma_{Z'} \times BR(Z' \to t\bar{t})$ for Z' heavier than 1.1 TeV/c^2, and we also exclude the Kaluza-Klein gluon model with $1.0 < M < 1.5\,\text{TeV}/c^2$.

We have also measured the subjet energy scale and substructure selection efficiency in data using the semileptonic sample, which is dominated by the $t\bar{t}$ events. In addition, performance of the top tagging and W tagging algorithms is illustrated in a sample of events passing the "1+2" selections with an additional b tagged jet requirement. A large number of boosted continuum $t\bar{t}$ is expected in this sample.

13 Acknowledgements

We wish to congratulate our colleagues in the CERN accelerator departments for the excellent performance of the LHC machine. We thank the technical and administrative staff at CERN and other CMS institutes, and acknowledge support from: FMSR (Austria); FNRS and FWO (Belgium); CNPq, CAPES, FAPERJ, and FAPESP (Brazil); MES (Bulgaria); CERN; CAS, MoST, and NSFC (China); COLCIENCIAS (Colombia); MSES (Croatia); RPF (Cyprus); Academy of Sciences and NICPB (Estonia); Academy of Finland, MEC, and HIP (Finland); CEA and CNRS/IN2P3 (France); BMBF, DFG, and HGF (Germany); GSRT (Greece); OTKA and NKTH (Hungary); DAE and DST (India); IPM (Iran); SFI (Ireland); INFN (Italy); NRF and WCU (Korea); LAS (Lithuania); CINVESTAV, CONACYT, SEP, and UASLP-FAI (Mexico); MSI (New Zealand); PAEC (Pakistan); SCSR (Poland); FCT (Portugal); JINR (Armenia, Belarus, Georgia, Ukraine, Uzbekistan); MST, MAE and RFBR (Russia); MSTD (Serbia); MICINN and CPAN (Spain); Swiss Funding Agencies (Switzerland); NSC (Taipei); TUBITAK and TAEK (Turkey); STFC (United Kingdom); DOE and NSF (USA). This work was supported in part by the DOE under under Task TeV of contract DE-FG02-96ER40956 during the Workshop on Jet Substructure at the University of Washington.

References

[1] S. Dimopoulos and H. Georgi, "Softly Broken Supersymmetry and SU(5)", *Nucl. Phys.* **B193** (1981) 150. doi:10.1016/0550-3213(81)90522-8.

[2] S. Weinberg, "Implications of Dynamical Symmetry Breaking", *Phys. Rev.* **D13** (1976) 974–996. doi:10.1103/PhysRevD.13.974.

[3] L. Susskind, "Dynamics of Spontaneous Symmetry Breaking in the Weinberg- Salam Theory", *Phys. Rev.* **D20** (1979) 2619–2625. doi:10.1103/PhysRevD.20.2619.

[4] C. T. Hill and S. J. Parke, "Top production: Sensitivity to new physics", *Phys. Rev.* **D49** (1994) 4454–4462, arXiv:hep-ph/9312324. doi:10.1103/PhysRevD.49.4454.

[5] R. S. Chivukula, B. A. Dobrescu, H. Georgi et al., "Top quark seesaw theory of electroweak symmetry breaking", *Phys. Rev.* **D59** (1999) 075003, arXiv:hep-ph/9809470. doi:10.1103/PhysRevD.59.075003.

[6] N. Arkani-Hamed, A. G. Cohen, and H. Georgi, "Electroweak symmetry breaking from dimensional deconstruction", *Phys. Lett.* **B513** (2001) 232–240, arXiv:hep-ph/0105239. doi:10.1016/S0370-2693(01)00741-9.

[7] N. Arkani-Hamed, S. Dimopoulos, and G. R. Dvali, "The hierarchy problem and new dimensions at a millimeter", *Phys. Lett.* **B429** (1998) 263–272, arXiv:hep-ph/9803315. doi:10.1016/S0370-2693(98)00466-3.

[8] L. Randall and R. Sundrum, "A large mass hierarchy from a small extra dimension", *Phys. Rev. Lett.* **83** (1999) 3370–3373, arXiv:hep-ph/9905221. doi:10.1103/PhysRevLett.83.3370.

[9] L. Randall and R. Sundrum, "An alternative to compactification", *Phys. Rev. Lett.* **83** (1999) 4690–4693, arXiv:hep-th/9906064. doi:10.1103/PhysRevLett.83.4690.

[10] K. Agashe, A. Belyaev, T. Krupovnickas et al., "LHC signals from warped extra dimensions", *Phys. Rev.* **D77** (2008) 015003, arXiv:hep-ph/0612015. doi:10.1103/PhysRevD.77.015003.

[11] Y. Bai, J. L. Hewett, J. Kaplan et al., "LHC Predictions from a Tevatron Anomaly in the Top Quark Forward-Backward Asymmetry", *JHEP* **1103** (2011) 003, arXiv:1101.5203. doi:10.1007/JHEP03(2011)003.

[12] P. H. Frampton, J. Shu, and K. Wang, "Axigluon as Possible Explanation for $p\bar{p} \to t\bar{t}$ Forward-Backward Asymmetry", *Phys. Lett.* **B683** (2010) 294–297, arXiv:0911.2955. doi:10.1016/j.physletb.2009.12.043.

[13] M. I. Gresham, I.-W. Kim, and K. M. Zurek, "On Models of New Physics for the Tevatron Top A_FB", *Phys. Rev.* **D83** (2011) 114027, arXiv:1103.3501. doi:10.1103/PhysRevD.83.114027.

[14] O. Antunano, J. H. Kuhn, and G. Rodrigo, "Top quarks, axigluons and charge asymmetries at hadron colliders", *Phys. Rev.* **D77** (2008) 014003, arXiv:0709.1652. doi:10.1103/PhysRevD.77.014003.

[15] R. M. Godbole and D. Choudhury, "Nonstandard, strongly interacting spin one t anti-t resonances", arXiv:0810.3635.

[16] CDF Collaboration, "Forward-Backward Asymmetry in Top Quark Production in ppbar Collisions at sqrts=1.96 TeV", *Phys. Rev. Lett.* **101** (2008) 202001, arXiv:0806.2472. doi:10.1103/PhysRevLett.101.202001.

[17] D0 Collaboration, "First measurement of the forward-backward charge asymmetry in top quark pair production", *Phys. Rev. Lett.* **100** (2008) 142002, arXiv:0712.0851. doi:10.1103/PhysRevLett.100.142002.

[18] CDF Collaboration, "Evidence for a Mass Dependent Forward-Backward Asymmetry in Top Quark Pair Production", *Phys. Rev.* **D83** (2011) 112003, arXiv:1101.0034. doi:10.1103/PhysRevD.83.112003.

[19] D0 Collaboration, "Measurement of the forward-backward production asymmetry of t and $\bar{t}$ quarks in $p\bar{p}tot\bar{t}$ events.", *D0 Note* **6062-CONF** (2010).

[20] CDF Collaboration, "Measurement of the Forward Backward Asymmetry in Top Pair Production in the Dilepton Decay Channel using 5.1 fb^{-1}.", *CDF Note* **10436** (2011).

[21] R. S. Chivukula, E. H. Simmons, and C. P. Yuan, "Axigluons cannot explain the observed top quark forward- backward asymmetry", *Phys. Rev.* **D82** (2010) 094009, arXiv:1007.0260. doi:10.1103/PhysRevD.82.094009.

[22] CDF Collaboration, "Limits on the production of narrow t anti-t resonances in p anti-p collisions at s**(1/2) = 1.96-TeV", *Phys. Rev.* **D77** (2008) 051102, arXiv:0710.5335. doi:10.1103/PhysRevD.77.051102.

[23] CDF Collaboration, "Search for resonant t anti-t production in p anti-p collisions at s**(1/2) = 1.96-TeV", *Phys. Rev. Lett.* **100** (2008) 231801, arXiv:0709.0705. doi:10.1103/PhysRevLett.100.231801.

[24] D0 Collaboration, "Search for $t\bar{t}$ Resonances in the Lepton+Jets Final State in $p\overline{p}$ Collisions at $\sqrt{s}$ = 1.96 TeV", *D0 Note* **5882-CONF** (2009).

[25] R. M. Harris, C. T. Hill, and S. J. Parke, "Cross-section for topcolor Z-prime(t) decaying to t anti-t: Version 2.6", arXiv:hep-ph/9911288.

[26] D. E. Kaplan, K. Rehermann, M. D. Schwartz et al., "Top Tagging: A Method for Identifying Boosted Hadronically Decaying Top Quarks", *Phys. Rev. Lett.* **101** (2008) 142001, arXiv:0806.0848. doi:10.1103/PhysRevLett.101.142001.

[27] CMS Collaboration, "*A Cambridge-Aachen (C-A) based Jet Algorithm for boosted top-jet tagging*", *CMS Physics Analysis Summary* **CMS-PAS-JME-009-01** (2009).

[28] S. D. Ellis, J. Huston, K. Hatakeyama et al., "Jets in hadron-hadron collisions", *Prog. Part. Nucl. Phys.* **60** (2008) 484–551, arXiv:0712.2447. doi:10.1016/j.ppnp.2007.12.002.

[29] S. D. Ellis, C. K. Vermilion, and J. R. Walsh, "Techniques for improved heavy particle searches with jet substructure", *Phys.Rev.* **D80** (2009) 051501, arXiv:0903.5081. doi:10.1103/PhysRevD.80.051501.

[30] S. D. Ellis, C. K. Vermilion, and J. R. Walsh, "Recombination Algorithms and Jet Substructure: Pruning as a Tool for Heavy Particle Searches", *Phys.Rev.* **D81** (2010) 094023, arXiv:0912.0033. doi:10.1103/PhysRevD.81.094023.

[31] A. Abdesselam, E. Kuutmann, U. Bitenc et al., "Boosted objects: A Probe of beyond the Standard Model physics", *Eur.Phys.J.* **C71** (2011) 1661, arXiv:1012.5412.

[32] CMS Collaboration, "The CMS experiment at the CERN LHC", *JINST* **3** (2008) S08004. doi:10.1088/1748-0221/3/08/S08004.

[33] CMS Collaboration, "Particle-Flow Event Reconstruction in CMS and Performance for Jets, Taus, and MET", *CMS PAS PFT-09-001* (2009).

[34] J. Alwall et al., "MadGraph/MadEvent v4: The New Web Generation", *JHEP* **09** (2007) 028, arXiv:0706.2334. doi:10.1088/1126-6708/2007/09/028.

[35] T. Sjostrand et al., "High-energy physics event generation with PYTHIA 6.1", *Comput. Phys. Commun.* **135** (2001) 238–259, arXiv:hep-ph/0010017. doi:10.1016/S0010-4655(00)00236-8.

[36] M. Wobisch and T. Wengler, "Hadronization corrections to jet cross sections in deep-inelastic scattering", arXiv:hep-ph/9907280.

[37] Y. L. Dokshitzer, G. D. Leder, S. Moretti et al., "Better Jet Clustering Algorithms", *JHEP* **08** (1997) 001, arXiv:hep-ph/9707323.

[38] M. Cacciari and G. P. Salam, "Dispelling the N**3 myth for the k(t) jet-finder", *Phys. Lett.* **B641** (2006) 57–61, arXiv:hep-ph/0512210. doi:10.1016/j.physletb.2006.08.037.

[39] M. Cacciari, G. P. Salam, and G. Soyez, "fastjet Package",.

[40] M. Cacciari, G. P. Salam, and G. Soyez, "The Catchment Area of Jets", *JHEP* **04** (2008) 005, arXiv:0802.1188. doi:10.1088/1126-6708/2008/04/005.

[41] M. Cacciari and G. P. Salam, "Pileup subtraction using jet areas", *Phys. Lett.* **B659** (2008) 119–126, arXiv:0707.1378. doi:10.1016/j.physletb.2007.09.077.

[42] CMS Collaboration, "Jet Energy Corrections determination at 7 TeV", *CMS PAS JME-10-010* (2010).

[43] CMS Collaboration, "Study of Jet Substructure in pp Collisions at 7 TeV in CMS.", *CMS Physics Analysis Summary* **CMS-PAS-JME-10-013**.

[44] J. M. Butterworth, A. R. Davison, M. Rubin et al., "Jet substructure as a new Higgs search channel at the LHC", *Phys. Rev. Lett.* **100** (2008) 242001, arXiv:0802.2470. doi:10.1103/PhysRevLett.100.242001.